Field line resonances in a cylindrical plasma

C. C. Mitchell, J. E. Maggs, and W. Gekelman
University of California, Los Angeles, California 90095-1696

(Received 17 December 2001; accepted 26 March 2002)

An experimental study of the response to an impulsive driver in a low beta helium plasma is presented. Field line resonance (FLR) spectra are recorded and compared to an ideal magnetohydrodynamic (MHD) theory with finite ion cyclotron frequency corrections. The agreement between observed and predicted values is generally within the frequency resolution of the measurements except for the lowest frequency harmonic. The spectrum of the lowest harmonic is compared to various ultra low-frequency (ULF) FLR dispersion relations. Dispersion effects due to nonzero perpendicular wave number are found to be important for the lowest frequency harmonic. Quality factors are measured and compared to theoretical estimates from a two-fluid theory with finite parallel electron temperature. Reflection coefficient values are obtained using measured and estimated Q values. © *2002 American Institute of Physics.* [DOI: 10.1063/1.1483310]

I. INTRODUCTION

Alfvén resonance, or field line resonance (FLR), has enjoyed attention from both fusion and space plasma communities. FLR heating schemes have been proposed, discussed, and refined by many authors. An introductory overview can be found in Hasegawa's technical report.[1] Experimental ion heating efforts have been carried out on both linear machines[2,3] and tokamaks,[4,5] but the focus of these experiments was on energy absorption rather than resonance spectra. On the other hand, space plasma physicists commonly observe low frequency resonant oscillations in the ionosphere.[6–9] FLRs have been observed at the onset of an auroral substorm,[8] and observations of FLRs prior to substorm onset may suggest a causal relationship between the two phenomena.[10,11] It has been suggested that FLRs are responsible for the formation of auroral arcs.[12,13] Various models of FLR boundary conditions in the Earth's ionosphere have also been proposed, including a magnetohydrodynamic (MHD) cavity mode model,[14] and a waveguide model.[15]

FLR has also been the subject of truculent jeremiads. The numerical consideration of a parallel density inhomogeneity (in addition to the standard transverse homogeneity considered in most introductory disquisitions) was claimed by Goertz[16] to remove the Alfvén resonance singularity from the equations by introducing a new mode coupling of the wave magnetic field components. This would suggest that a large amount of the literature in the fields of solar corona heating, laboratory plasma heating, and magnetospheric pulsations is wrong. The claim was, of course, refuted.[17–19] Goertz then again attempted to invalidate the two-dimensional FLR expansion with a rebuttal, but his life was tragically cut short.[20]

The stakes of the debate were raised when the entire FLR concept was called ''invalid'' by Bellan[21] 2 years later. Bellan launched a two-pronged attack aimed primarily at the fusion community: one which attempted to invalidate the ideal MHD derivation of FLR and another two-fluid argument. His assertions were vigorously attacked,[22–24] and Bellan retracted his ideal MHD criticism,[25] but continued to advocate his two-fluid objections[26]—this time primarily in the context of space plasma physics. The response of the space plasma community was that while Bellan's extensive ''exact,'' cold, two-fluid equations are algebraically correct, they are irrelevant when the time scales of magnetospheric phenomena are considered,[27], and that plasma dissipation processes lead to well-behaved resonances.[28,29]

In contrast to its colorful history, FLR frequency spectra have quietly and consistently been a valuable tool for the space community. Spacecraft observations have been used to infer equatorial ion mass densities[30] and continue to be so used extraterrestrially.[31] Finding an isolated harmonic on Mercury, Russell[32] estimated the length of the field line and its electron density, assumed the ions were protons, and concluded that the resonance observed was a fourth-order harmonic. Harmonic values of FLRs in Earth's magnetosphere have been similarly determined.[33]

After a brief synopsis of the experimental arrangement, this paper compares a simple recursive formula to the frequency spectra obtained from magnetic probes in several ambient magnetic fields. The lowest harmonic of the spectrum in a 1000 G field is compared with two ULF FLR dispersion formulas presented in recent papers as well as with a kinetic formulation. Experimental Q (quality factor) values are contrasted with theoretical Q values obtained from a two-fluid theory with finite parallel electron temperature, and the differences between these values are used to acquire a reflection coefficient for the five lowest frequencies in the spectrum.

II. EXPERIMENT

A. The large plasma device

The work presented in this paper was undertaken in the LArge Plasma Device, or LAPD,[34] which provides a large enough plasma to facilitate the study of Alfvén waves. The LAPD is a 10 m long, 1 m diameter stainless-steel cylinder

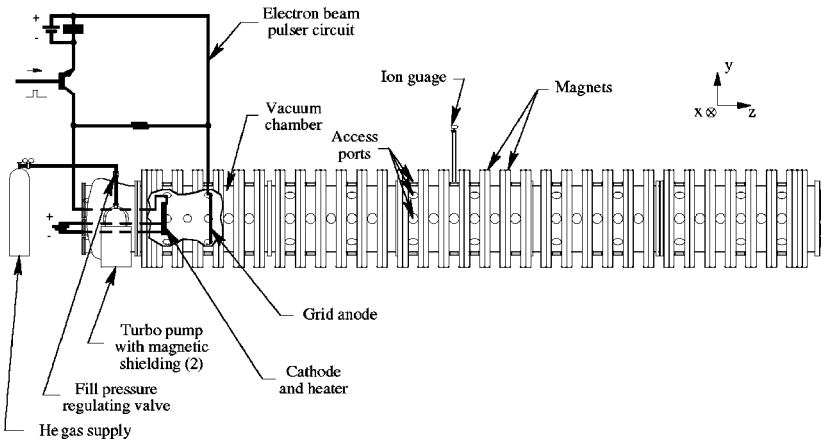

FIG. 1. Schematic of the LAPD showing plasma discharge source.

with a pulsed plasma source capable of producing a quiescent plasma hundreds of ion Larmor radii across. A diagram of the LAPD is show in Fig. 1.

Typical discharge currents last about 5 milliseconds and can exceed four thousand amperes. The cathode is pulsed once per second, and the bulk density variation of the plasma from shot to shot is approximately 5%. Density and temperature measurements are acquired at various axial locations in the LAPD via Langmuir probe measurements,[35] and calibrated with a 57 GHz microwave interferometer.[36]

B. Wave excitation and detection

A phase-locked, one-cycle sine wave burst with a frequency equal to half the ion cyclotron frequency served as the driver. This input signal was chosen for its broadband Fourier spectrum, encouraging the excitation of many eigenmodes.

The antenna (labeled ''blade antenna'') can be seen on the right-hand side of Fig. 2. It is in the shape of a rectangle's perimeter with one side removed: two sides are perpendicular to the ambient **B** field and one side is parallel. The perpendicular legs can be moved radially to adjust the position of the parallel leg relative to the **B** axis. The parallel leg is aligned (by eye) with the center of the machine—i.e., along the z axis at $r=0$. The antenna is a solid copper cylinder 0.64 cm in diameter and 91.8 cm in length. The diameter corresponds to approximately 1.5 electron skin depths in this experiment, $\delta=c/\omega_{pe}$, where c is the speed of light, and ω_{pe} is the electron plasma frequency. The radiation patterns of Alfvén waves excited by antennas with transverse lengths comparable to the electron skin depth have been discussed by Morales[37] and studied experimentally by Gekelman.[38]

The antenna receives an excitation pulse from an rf power amplifier via a 1:1 transformer. The impulse flows only in the loop defined by the three legs of the antenna, so it is the sole source of wave energy. The current in the long leg aligned along $\hat{z}$ has an amplitude of ≈ 1.5A peak to peak, and creates an azimuthal magnetic induction.

The magnetic field of waves excited by the impulse is measured by a probe comprising three orthogonally oriented 8-mm-diameter induction coils which is sensitive to the time derivative of the magnetic field.[39] This receiver is mounted on the end of a 0.64 cm diameter stainless-steel shaft. The shaft is connected to the machine through a ball joint which is used in the experiments presented here to obtain planar data normal to the magnetic field axis.

The receiver is differential, in that each axis consists of two oppositely wound coils of 50 turns each. This allows a differential amplifier to select magnetic signal and reject common mode noise. At each spatial location several plasma shots are recorded. The three components of the magnetic field are captured simultaneously, their amplitude variations digitized in a time window, and recorded on computer disk.[40]

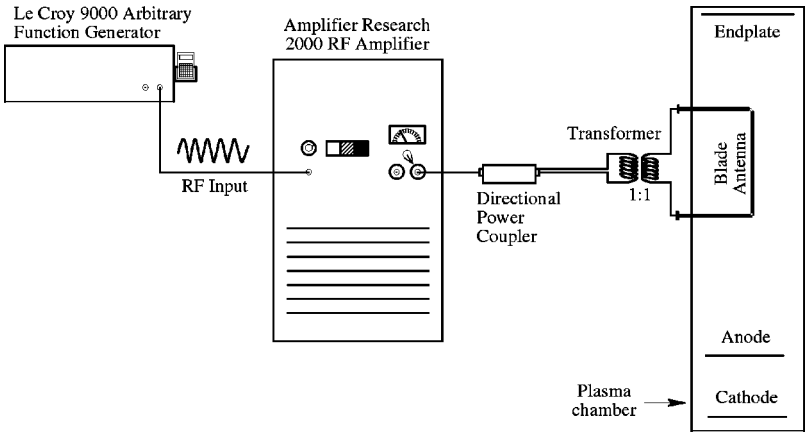

FIG. 2. Schematic of experimental setup (not to scale) showing the ''blade'' antenna.

III. EXPERIMENTAL RESULTS

A. Overview

In this section we investigate laboratory observations of shear Alfvén wave resonances with a helium plasma in the LAPD. Power spectrum data are presented which show the existence of many standing eigenmodes in the shear Alfvén frequency range, and this is obtained for ten distinct ambient magnetic fields. Harmonic frequency dependence on ambient $\mathbf{B}_0$ is presented for three resonant frequencies, and shows the linear dependence on $\mathbf{B}_0$ expected for a shear Alfvén wave. The spectrum agrees very well with a recursive dispersion relation which assumes a standing Alfvén wave and a plasma with finite ion cyclotron frequency. Experimental Q values for the first five eigenfrequencies are measured and compared to theoretical Q values, and a reflection coefficient is obtained from these Q values. An abridged synopsis of a subset of the results presented here has already been published.[41]

B. Spectral analysis

The object of this experiment is to excite a broadband Fourier spectrum in order to observe the natural Alfvén modes of the plasma. If these modes are standing waves, we can assume that $\lambda_n = 2L/n, n = 1,2,\ldots,$ where L is the length of the plasma column in the LAPD (8.95 m). We now need a dispersion relation from which we can obtain an expression for the eigenfrequencies.

The plasma parameters relevant to the dispersion relation are the thermal to magnetic energy ratio, $\beta = 8\pi nkT_e/B_0^2$, and the ion sound gyroradius, $\rho_s = c_s/\Omega_{ci}$. Since $\beta \gtrsim 3m_e/M_I$, the wave is kinetic, and since $k_\perp \rho_s \lesssim 0.2$, finite ion sound gyroradius effects can be neglected. This means that the dispersion relation for the shear wave can be written with only a finite ion cyclotron frequency correction to the ideal MHD case

$$\omega/k_\parallel = v_A(1-\omega^2/\Omega_{ci}^2)^{1/2}, \tag{1}$$

where $v_A = B_0/(4\pi Mn)^{1/2}$. This is the dispersion relation which will be used to predict standing mode eigenfrequencies in the LAPD.

We now wish to solve Eq. (1) for the eigenfrequencies, f_n. We find

$$f_n = \frac{v_A}{\sqrt{(4L^2/n^2 + v_A^2/f_{ci}^2)}}. \tag{2}$$

From this expression, a recursion relation for the nth eigenfrequency in terms of the jth eigenfrequency can be obtained. Its only fundamental dependence in terms of plasma parameters is on f_{ci}

$$f_n^2 = f_j^2 n^2/(j^2 + (n^2 - j^2) f_j^2/f_{ci}^2). \tag{3}$$

Qualitatively, Eq. (3) implies that for a given j, f_j, the successive eigenfrequencies f_n will get increasingly closer as $f_n \to f_{ci}$, and this is indeed observed in the data.

Data showing wave magnetic response power spectra obtained for three different values of the background magnetic field are given in Figs. 3–5.

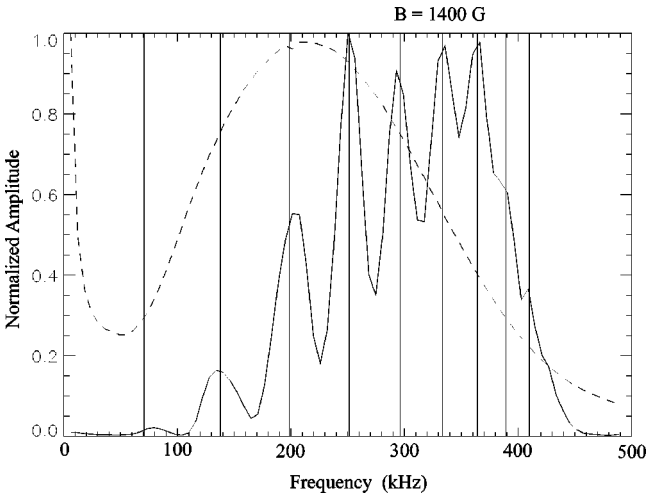

FIG. 3. The frequency spectrum of the magnetic response for $B_0 = 1400$ G is shown as the solid curve above. The vertical bars are theoretical predictions of the peak frequencies, and the dotted curve is the power spectrum of the exciter. $f_{ci} = 536.2$ kHz, $f_j = 248.6$ kHz, $j = 4$, and the five lowest harmonics have (from left to right) $Q = 2.8,3.9,5.8,8.2,10.2$.

The vertical bars that overlap resonances are acquired from Eq. (3). They are obtained by looking at a Fourier spectrum of wave magnetic field data, picking a peak (f_j), counting the number of peaks preceding it to determine the harmonic number (j), and finally calculating the f_n corresponding to each n. The broken line in each plot is the antenna power spectrum. The solid curve is the frequency response of $\mathbf{B}_\perp$, uncorrected for antenna input power, and digitally integrated from the raw $d\mathbf{B}/dt$ signal recorded by the DAQ (Data AcQuisition system). The caption of each graph gives f_{ci} for that $\mathbf{B}_0$, and the values used to determine the overplotted lines. For example, in Fig. 3, the peak located near 248 kHz was estimated to have a harmonic value of 4, since three peaks were visible at lower frequencies. These two values are inserted into Eq. (3) to determine the remaining vertical bars (f_n) shown. Each caption also includes the

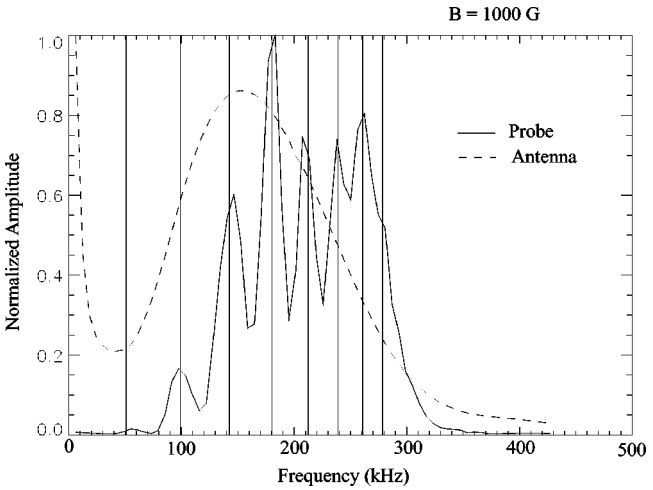

FIG. 4. Power spectrum for $B_0 = 1000$ G, $f_{ci} = 383.0$ kHz, $f_j = 238.0$ kHz, $j = 6$, $Q = 2.4,4.1,5.3,9.5,10.0$.

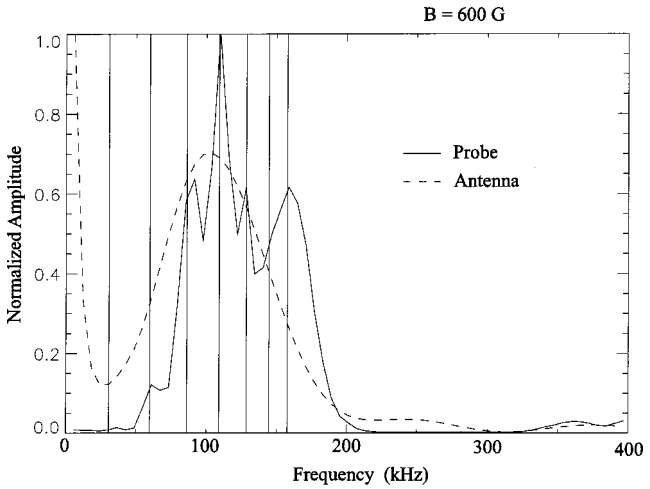

FIG. 5. Power spectrum for $B_0=600$ G, $f_{ci}=229.8$ kHz, $f_j=109.1$ kHz, $j=4$. There is insufficient spectral resolution to determine Q for the first five harmonics.

Q values obtainable directly from the power spectrum. For each ambient magnetic field, the Q values become unresolvable after the fifth harmonic.

The given perpendicular magnetic field response is acquired at one representative spatial point near the center of the column over ambient magnetic field values ranging from 1400G→600 G. At each spatial point 200 plasma discharges were recorded, and the average over all shots is plotted as the response shown in Figs. 3–5. The data have been corrected for probe frequency response.

Looking first at Fig. 3, there is a clear drop in energy before the 536 kHz cyclotron frequency shear Alfvén wave cutoff, and for all ambient magnetic fields in which this experiment was performed the cyclotron cutoff is clearly manifest.

Equation (3) predicts an infinite number of harmonics with decreasing separation as $f\rightarrow f_{ci}$, but only the first nine harmonics are shown here since no experimental peaks are resolved after $n=9$. The good agreement between theory and experiment is clear for the first seven harmonics, and even though the experimentally obtained spectral peaks are not as clearly resolved at the $n=8$ and $n=9$ harmonics, one can still see that the vertical lines of the theoretical prediction intersect the measured spectrum at peak locations.

As indicated by Eq. (3), the eigenmodes ''pile up'' near the Ω_{ci} cutoff. This trend is especially apparent for the $n=7,8,9$ harmonics in the ambient fields of 1400 G. This occurs to some degree for every field investigated, but is more clearly described for the higher ambient magnetic fields. The interpeak frequency separation decreases with decreasing ambient $\mathbf{B}_0$, so higher harmonics are washed out as the ambient $\mathbf{B}_0$ decreases.

The power spectra of the input signal and the detected probe response are plotted with normalized amplitudes in order to be viewed on the same graph. In this way, it is clear that the amplitude of the input at a given frequency does not necessarily determine the amplitude of the response. As an example, consider the $n=2$ and $n=5$ peaks of the 1400 G response shown in Fig. 3. While both harmonics have roughly the same input power, the $n=5$ peak has almost 6 times the power of the $n=2$ peak. This effect is also very evident in the case of the 600 G field shown in Fig. 5. Here, the response of the $n=7$ harmonic is larger than the sixth and comparable to the fifth even though the source strength is rapidly decreasing in this frequency range. Evidently, the plasma dumps energy into the most favorable modes, not necessarily the modes encouraged by the input pulse.

The frequency resolution at each harmonic is determined by the duration of the signal. Since the temporal duration of the higher harmonics is less than the lower harmonics, the frequency resolution is generally poorer for the higher harmonics. The frequency resolution for the higher harmonics ($n\geqslant 3$) is ± 5 kHz, while the resolution for the first two harmonics is ± 2.5 kHz. The observed deviations of the higher harmonics from the predicted values are, for the most part, within the frequency resolution of the measurements. However, for all the magnetic fields investigated, the $n=1$ peak in each case departed the most from the recursive formula given above. Also, the deviation of the observed value from the predicted value exceeds the frequency resolution limits. Therefore, it is informative to investigate the effects of corrections to the dispersion relation that depend on perpendicular wavelength for the $n=1$ case. Since an entire plane of data was acquired in the case of ambient $\mathbf{B}_0=1000$ G, we can extract perpendicular wavelength information from the data and attempt to reconcile this inconsistency in the lowest harmonic by considering the related dispersive effects.

Closer inspection of the fundamental harmonic than is available in Fig. 4 gives an experimental value for f_0 of 54.8 kHz ± 2.5 kHz, while the recursive formula predicts a value of $f_0=50.4$ kHz. In the frequency range of the fundamental harmonic $\omega\ll\Omega_{ci}$, so we can assume $\overline{\omega}\approx 0$. A relevant dispersion relation for ULF FLRs has been obtained by Streltsov.[42] He presents a two-fluid theory using a dimensionless vector potential $\mathbf{A}$ to determine the perturbed magnetic field and a perturbed electrostatic potential ϕ. For the low-beta, cold ion plasma case, the same dispersion relation is obtained in a more extensive analysis by Hollweg.[43] The dispersion relation so obtained can be written as

$$\omega^2=k_\parallel^2 v_A^2\frac{1+(\beta k_\perp^2\delta_i^2/2)}{1+k_\perp^2\delta_e^2}, \tag{4}$$

where δ is the plasma skin depth of the ions and electrons.

Equation (4) considers both finite electron inertia and finite electron pressure, i.e., inertial and kinetic effects. From density and temperature measurements taken as described in Sec. II A, we observe $n_e=1.43\times 10^{12}$ cm^{-3}, $T_e=7.8$ eV and $T_i=1.0$ eV, giving, with $B_0=1000$ G, $\beta=4.5\times 10^{-4}$, $\delta_e=0.44$ cm, $v_{A0}=9.1\times 10^7$ cm/s, $\delta_i=38$ cm. Also, we have $k_\parallel=n\pi/L=0.0035$ cm^{-1} with $n=1$ for the fundamental parallel wave number. The $k_\perp$ values must be extracted from the data by Bessel function decomposition.

In order to acquire $k_\perp$ values, we must digitally filter the data to isolate the fundamental harmonic and then interpolate this data onto the radial rays of a polar coordinate plane. Two planes are shown for comparison: one of filtered and the

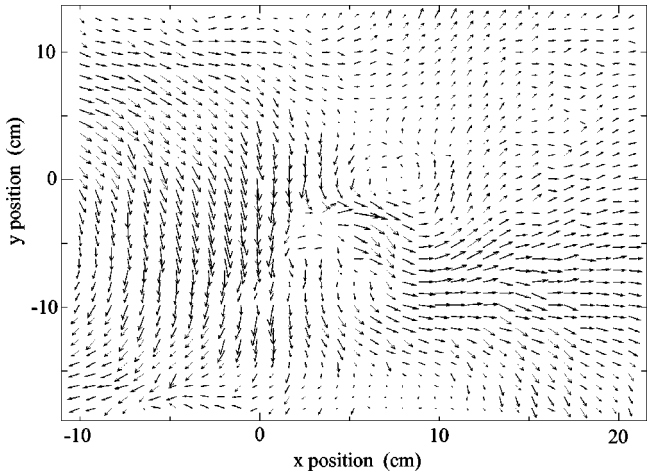

FIG. 6. Magnetic field data 9.4 μs after the beginning of the excitation pulse is shown before digital filtering. Multiple interference patterns from the many waves corresponding to the peaks of the spectral pattern of Fig. 4 are visible.

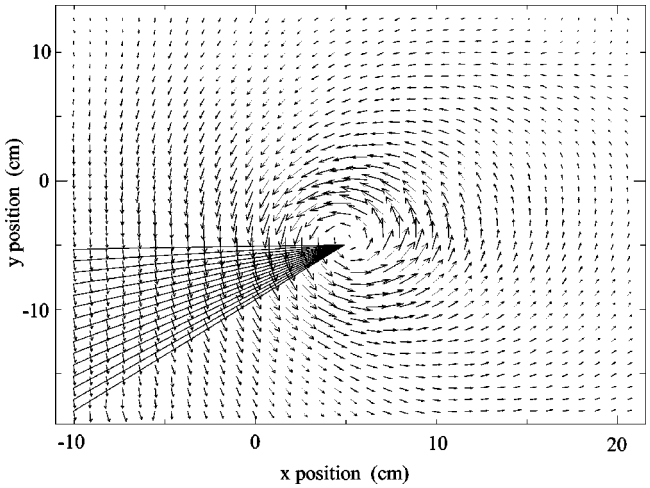

FIG. 8. Digitally filtered magnetic field data 8.16 μs after the beginning of the excitation pulse is shown overplotted with 15 radial arcs emanating from the wave center terminating in quadrant III of the rectangular grid defined by the DAQ. An entire plane of such rays defines the polar coordinate grid onto which the data are interpolated.

other of unfiltered data, each corresponding to $t=9.4$ μs after source turn-on. These can be seen in Figs. 6 and 7. Since each peak in Fig. 4 is a wave with its own phase and group velocities, their superposition (seen in Fig. 6) creates multiple interference patterns. Figure 7 shows the clear spatial pattern of the fundamental harmonic, which has been gleaned by digital filtering.

In addition to digital filtering, interpolation of the filtered data is necessary because the computer-controlled data acquisition system was programed to obtain rectangular, regularly spaced grids of magnetic field data. The center of the polar coordinate system is the center of the wave, determined by inspection of the magnetic vector field. The radial rays of this polar coordinate system terminate on the perimeter of the rectangle of spatial data points acquired by the DAQ, as shown in Fig. 8. Magnetic field data 8.16 μs after the beginning of the excitation pulse are shown overplotted with 15 radial arcs emanating from the wave center—which is defined by a click of the mouse. The time chosen for this figure represents a peak in wave intensity. Since the rectangular plane is 35×35, we will have 140 radial profiles after interpolating the data onto every radial arc. Every radial arc contains B_ϕ and B_r information.

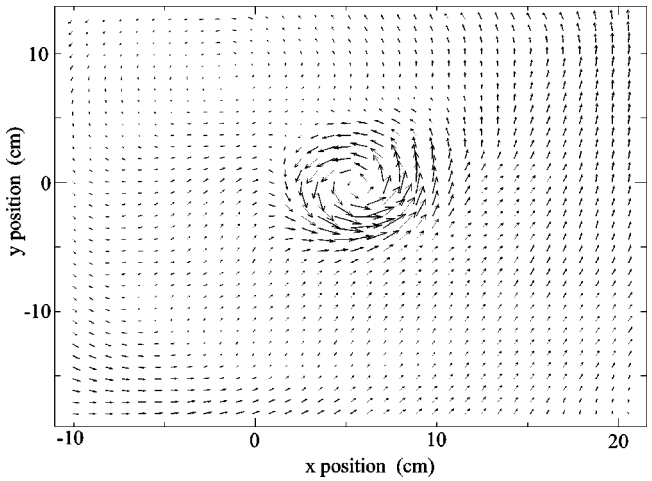

FIG. 7. Magnetic field data 9.4 μs after the beginning of the excitation pulse is shown after digital filtering. The fundamental peak has been extracted from the interference patterns of Fig. 6.

Each radial arc obtained in the plane at a time when the amplitude is largest is subjected to Bessel function decomposition. This procedure returns a spectrum of $k_\perp$ values and weighting coefficients. The Bessel coefficients were obtained numerically by using formula 11.52 in Arfken[44]

$$c_{n\nu}=\frac{2}{a^2[J_{n+1}(\alpha_{n\nu})]^2}\int_0^a f(\rho)J_n\left(\alpha_{n\nu}\frac{\rho}{a}\right)\rho\,d\rho, \tag{5}$$

where $\alpha_{n\nu}$ is the νth zero of J_n and $\alpha_{n\nu}/a=k_\perp$. Since the value of $\alpha_{n\nu}$ is predetermined by the inherent properties of J_n, the statement that $k_\perp$ values depend on the basis used is equivalent to stating that they depend on the choice of plasma boundary, a. Since the plasma boundary cannot be precisely known, but only estimated from the density profile for this experiment, there will be some uncertainty in the experimentally mined $k_\perp$ values.

After Bessel decomposition of each of the 140 radial arcs, an average $\langle k_\perp\rangle=0.55$ cm^{-1} with a standard deviation of $\delta k_\perp=0.025$ cm^{-1} is obtained. This value of $k_\perp$ used in Eq. (4) leads to a predicted fundamental frequency, $f_0=52.3$ kHz. This value is less than, but within the experimental uncertainties of, the observed frequency mentioned previously (54.8 ± 2.5 kHz).

Streltsov's two-fluid theory has recently been criticized by Battacharjee[45] for failing to include parallel ion flow and finite ion temperature. Battacharjee gives a four-field theory to describe ULF FLRs in the ionosphere, which includes, in addition to $\mathbf{A}$ and ϕ, a perturbed electron pressure p and a perturbed parallel ion speed v. This four-field model is supposed to better account for low-frequency FLRs. The dispersion relation that Battacharjee gets can be written as

$$\left(\frac{\omega_{\pm}}{k_{\|}v_A}\right)^2 \approx \frac{1}{2(1+k_\perp^2\delta_e^2)}\left[1+\frac{1}{2}\beta(1+\tau)+\left(\frac{1+\tau}{2\tau}+\frac{\beta\tau}{16}\right)k_\perp^2\rho_i^2\right] \pm\frac{1}{2(1+k_\perp^2\delta_e^2)}\left[1-\beta(1+\tau)+\left(\frac{1+\tau}{\tau}+\frac{\beta\tau}{8}+\frac{\beta(1-\tau^2)}{2\tau}\right)k_\perp^2\rho_i^2\right]^{1/2}, \quad (6)$$

where $\tau \equiv T_i/T_e$ is the ratio of ion temperature to electron temperature. Equation (4) can be recovered from the linear four-field equations leading to Eq. (6) by setting $\tau=0$ and neglecting parallel ion flow v and ion gyroradius ρ_i. Inserting the same experimental values as before (and $T_i=1$ eV), the predicted fundamental harmonic is $f_0=52.7$ kHz, which is indeed closer to the observed value. Although Battacharjee's value is nominally closer to the observed frequency, both are an improvement over the 50.4 kHz value predicted by Eq. (1), and both are within the experimental uncertainty of the observed value.

The above dispersion relations come from fluid descriptions of the plasma. The fluid picture is the one most commonly used to explain Alfvén resonance in space. We may compare these formulas with the full kinetic electron dispersion relation, which can be written as[46]

$$Z'(\zeta)\left[\frac{m}{M\beta}\left(1-\frac{\omega^2}{\Omega_{ci}^2}\right)-\zeta^2\right]=k_\perp^2\delta_e^2, \quad (7)$$

where $\zeta=\omega/k_{\|}v_e=(\omega/k_{\|}v_A)\sqrt{m/M\beta}$, and Z' is the derivative of the plasma dispersion function. Numerical solution of Eq. (7) for $B_0=1000$ G gives $\zeta=0.602$, which corresponds to $f=55.6$ kHz. This value is very close to the observed frequency. Kinetic ion dispersion[46–48] could also be included in Eq. (7), but, since the electrons are much hotter than the ions, the corrections are on the 1 percent level.

The above discussion has shown that even though the prediction of the recursive formula [Eq. (3)] with the fundamental harmonic is close, the small discrepancy that does exist can still be improved upon by considering dispersive effects due to finite $k_\perp$. Furthermore, by comparing the two dispersion relations [Eqs. (4) and (6)], it is shown that parallel ion flow and finite ion temperature are not important factors in the behavior of the fundamental harmonic in this experiment.

The excellent agreement between the experimental results and the recursive frequency relation in Eq. (3) suggests that FLR spectra can be used as a diagnostic tool for density measurement. Since ambient **B**, atomic species, and plasma dimensions are typically known quantities in laboratory plasmas, Eq. (1) can be used to solve for an axially averaged n_e. One simply reads the measured peak frequencies, f_n, off the Fourier spectrum and uses $\lambda_n=2L/n$ to solve for density. The numerous Langmuir measurements required to compare this prediction to an experimentally obtained column-length density average were not taken in this experiment. However, this technique agrees to within experimental uncertainty with the average density measured across the column using a 57 GHz microwave interferometer.

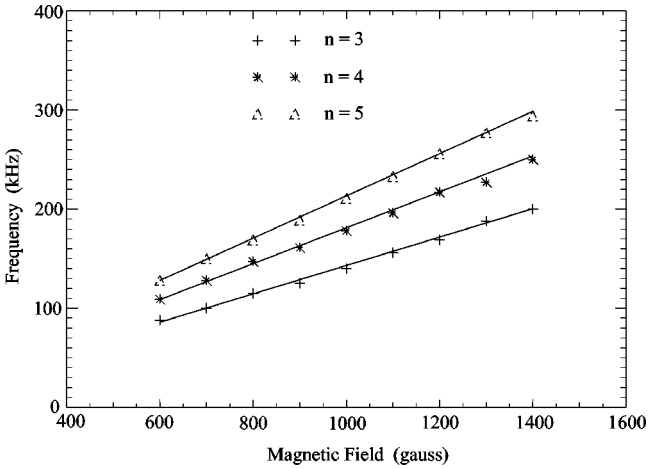

FIG. 9. Harmonic frequency dependence on external magnetic field value is plotted for $n=3$, 4, 5. The solid lines represent the predicted trend from Eq. (8).

C. Harmonic dependence on ambient B_0

Although the wave response was recorded for ten different ambient magnetic fields, only three were plotted in the interest of brevity. The FLR spatial properties do not change much with magnetic field, but the resolution in frequency becomes increasingly poor as Ω_{ci} decreases. Still, since we have the wave response in ten different magnetic fields, we are in a position to examine the dependence of an individual harmonic on the ambient $\mathbf{B}_0$. If we rewrite Eq. (2),

$$f_n=\frac{v_A}{\sqrt{(4L^2/n^2+c^2/f_{pi}^2)}}\propto B_0, \quad (8)$$

it is clear that the frequency of a given harmonic should increase linearly with external $\mathbf{B}_0$. A plot showing that this is indeed the case is given in Fig. 9.

D. Quality factor

An indication of the sharpness of the resonances is obtained by measuring their Q values, which are defined to be 2π times the ratio of the time-averaged energy stored in the cavity to the energy loss per cycle[49]

$$\frac{dU}{dt}=\frac{-\omega}{Q}U. \quad (9)$$

Theoretical Q values are computed by solving for the imaginary part of $k_\perp$ using a two-fluid dispersion relation including finite parallel electron temperature and collisional damping. The details of the derivation are relegated to the Appendix; the dispersion relation so obtained gives the following $k_\perp$:

$$k_\perp^2=\frac{\left[(\epsilon_{rr}+\epsilon_{zz})\left(\frac{\omega^2}{c^2}\epsilon_{rr}-k_\parallel^2\right)-\frac{\omega^2}{c^2}\epsilon_{r\phi}^2\right]}{2\epsilon_{rr}}\pm\frac{\sqrt{\left[(\epsilon_{rr}+\epsilon_{zz})\left(\frac{\omega^2}{c^2}\epsilon_{rr}-k_\parallel^2\right)-\frac{\omega^2}{c^2}\epsilon_{r\phi}^2\right]^2-4\epsilon_{rr}\epsilon_{zz}\left[\left(\frac{\omega^2}{c^2}\epsilon_{rr}-k_\parallel^2\right)^2-\frac{\omega^4}{c^4}\epsilon_{r\phi}^2\right]}}{2\epsilon_{rr}}. \tag{10}$$

The positive root of Eq. (10) corresponds to the compressional Alfvén wave, and the negative root to the shear wave. This can be seen most easily by considering low frequencies. If $\omega\ll\Omega_{ci}$, then neglecting ω also eliminates the $\epsilon_{r\phi}$ term from Eq. (10). The positive root can then be written, after some straightforward reductions, as $k_{+\perp}^2=(\omega^2/v_A^2)-k_\parallel^2$, which is just the cold two-fluid compressional wave dispersion. Similarly, if we neglect collisions and make the kinetic approximation $\omega^2\ll v_e^2k_\parallel^2$, then the negative sign reduces to $k_{-\perp}^2=(\omega^2/v_A^2k_\parallel^2-1)/\rho_s^2$, which is recognized as the dispersion relation for the shear Alfvén wave in the kinetic regime.

In the LAPD under these experimental conditions, the dominant damping factor is electron–ion collisions,[46] so we will make the approximation $\nu\equiv f_{ei}$. An electron–ion Coulomb collision frequency with velocity-independent collision operator has been given by Koch[50]

$$f_{ei}=\frac{2\pi ne^4\ln\Lambda}{m_e^2v_e^3}, \tag{11}$$

where $\Lambda\equiv 3/2(\kappa^3T^3/\pi n_e)^{1/2}$ is the Coulomb constant, and $v_e=\sqrt{(2kT_e/m_e)}$ is the electron thermal velocity. In this experiment, $\ln\Lambda\approx 12$.

After deciding on a damping model, theoretical Q values are obtained by filtering the peak in question from the power spectrum shown in Fig. 4. From this, a Bessel decomposition leads to a $k_\perp$ value in the manner discussed in Sec. III B. Treating the problem as a convective instability, we may write $\mathrm{Im}(\omega_n)=-\mathrm{Im}(k_n)\times\mathrm{Re}(v_{gn})$, where v_g is the group velocity, n indicates the eigenvalue of the harmonic, and Re and Im designate real and imaginary parts, respectively. This reduces the task of root finding in the complex plane to simply solving for the imaginary part of $k_\perp$ in Eq. (10) and computing $\mathrm{Im}(\omega_n)$. From this we may write an expression for the theoretical quality factor value, Q_{the}, by using the solution to Eq. (9), which defines Q, to obtain $Q_{\mathrm{the}}=\omega_{R,n}/2\omega_{I,n}$.

Theoretical Q values can be compared with experimental Q values obtained directly from the power spectrum. From the definition of Q in Eq. (9), we may obtain $Q_{\mathrm{exp}}=\omega/\Gamma$, where ω is the observed frequency and Γ is the full width of the resonance line at the half power point. Looking at Fig. 4, it is clear that experimental estimates of Q may only be obtained reliably for the first five harmonics, since the resolution of the power spectrum prohibits measurement of the half width after $n=5$. A comparison of these Q values is given in Table I.

It is evident that higher frequencies have higher Q values, and a wavelet analysis which shows that the lower frequencies live longer temporally but manifest fewer cycles has already been published.[41] Since the assumption $\nu\equiv f_{ei}$ neglects end losses at the anode and end plate—the node points of the standing wave—we expect the theoretical Q values to be well above the experimentally observed values.

E. Reflection coefficient

If we attribute the difference in Q values from experiment and theory solely to end losses in the machine, neglecting radial losses, we can get a rough estimate of the reflection coefficient, R. We do this by first refining our theoretical estimate of Q. This is accomplished by inserting into Eq. (9) a model for the decay of the stored energy, $U(t)$, which considers both plasma dissipation and end losses. By approximating this new theoretical Q, Q_{the}, with the experimentally obtained Q, Q_{exp}, we can obtain a soluble equation for R.

The previous theoretical estimate of Q was based solely on plasma dissipation

$$Q_{\mathrm{dis}}=\frac{\mathrm{Re}(\omega)}{2\,\mathrm{Im}(\omega)}=\frac{\mathrm{Re}(\omega)}{2\gamma}, \tag{12}$$

where γ is the imaginary part of the complex angular frequency, corresponding to energy losses which decay like $e^{-2\gamma t}$. We can refine this estimate of Q by considering that end losses in the machine result in a decrease in energy upon each reflection that can be modeled as $e^{-(1-R)v_gt/L}$, where v_g is the parallel group velocity, and L is the length of the plasma column. We may obtain v_g by taking the derivative of Eq. (1):

$$v_g=\frac{\partial\omega}{\partial k}=\frac{v_A\sqrt{1-\bar{\omega}^2}}{1+\frac{\omega k v_A}{\Omega^2\sqrt{1-\bar{\omega}^2}}}. \tag{13}$$

Since the group velocity depends on the harmonic number through the parallel wave number $k=n\pi/L$, Eq. (13) shows v_g decreasing with increasing harmonic.

TABLE I. Theoretical and experimental Q values at 1000 G for the first five harmonics.

Harmonic	f/f_{ci}	Q_{the}	Q_{exp}
1	0.146	6.0	2.4
2	0.254	13.6	4.1
3	0.373	18.5	5.3
4	0.472	22.8	9.5
5	0.555	31.7	10.0

TABLE II. Estimated reflection coefficients for the first five harmonics.

Harmonic	f/f_{ci}	R
1	0.146	0.568
2	0.254	0.449
3	0.373	0.276
4	0.472	0.511
5	0.555	0.236

Considering both end losses and plasma dissipation losses, we can write the decay of stored energy as a function of time as follows:

$$U(t)=U_0 e^{-(1-R)v_g t/L-\omega t/Q_{\rm dis}}. \tag{14}$$

If we substitute this model for stored energy decay in Eq. (9), we will obtain the new theoretical Q value, $Q_{\rm the}$:

$$Q_{\rm the}=\frac{\omega}{(1-R)\dfrac{v_g}{L}+\dfrac{\omega}{Q_{\rm dis}}}. \tag{15}$$

If we approximate $Q_{\rm the}$ by the $Q_{\rm exp}$ obtained directly from the power spectrum, we can obtain an expression for the reflection coefficient by solving for R in Eq. (15):

$$R=1-\frac{\omega L}{v_g}\left(\frac{1}{Q_{\rm exp}}-\frac{1}{Q_{\rm dis}}\right). \tag{16}$$

The R values obtained from this equation are given in Table II.

The values of R obtained with this technique are suspiciously low and somewhat erratic. One would expect a good conductor, like the copper end plate, to have a larger reflection coefficient less dependent upon frequency. It is likely that the obtained R values are inaccurate, but this speculation can be established only by a separate experiment.

IV. SUMMARY AND CONCLUSIONS

A rich spectrum of standing shear Alfvén waves, or field line resonances, excited by an impulsive driver were observed in a cylindrical, helium plasma column. The spacing between the observed resonant frequencies fit the pattern predicted from a two-fluid, kinetic Alfvén wave dispersion relation. Also, as expected, the resonant frequencies increased linearly with background magnetic field strength, over a range of 600→1400 Gauss. The measured quality factor, Q, of the resonances varied with field strength and resonant frequency, ranging in value from 2→10. The value of Q increases with increasing resonant frequency. While the observed Q values are somewhat low for resonant phenomena, they are generally larger than values observed in space plasmas.[51] The experimentally obtained Q values were consistently lower than values predicted from a two-fluid, finite parallel-electron-temperature theory with Coulomb collisional dissipation. Assuming this discrepancy arose from end losses, a model for reflection from the ends of the machine was used to estimate the reflection coefficient, R. Unexpectedly low, and somewhat unsystematic values for R were obtained, indicating that the technique used for finding the reflection coefficient is suspect.

The verification of the general properties of standing Alfvén wave resonances is of particular importance to the space plasma community, because they have used these resonances to infer global properties of plasmas both terrestrially and near solar system moons and planets.

ACKNOWLEDGMENTS

The authors acknowledge Professor George Morales for many useful discussions.

This work was supported by the Office of Naval Research and the DOE under Grant No. DE-FG03-00ER54598/A00.

APPENDIX: TWO-FLUID DERIVATION OF PERPENDICULAR WAVE NUMBER IN A CYLINDER WITH FINITE PARALLEL ELECTRON TEMPERATURE

The basic starting point is the linearized electron and ion fluid motion equations

$$n_0 m_e \frac{\partial \mathbf{v}_e}{\partial t}=-en_0\left(\frac{\mathbf{v}_e}{c}\times\mathbf{B}_0+\mathbf{E}\right)-\nabla p_e-n_0 m_e \nu \mathbf{v}_e, \tag{A1}$$

and

$$n_0 m_i \frac{\partial \mathbf{v}_i}{\partial t}=en_0\left(\frac{\mathbf{v}_i}{c}\times\mathbf{B}_0+\mathbf{E}\right)-n_0 m_i \nu \mathbf{v}_i, \tag{A2}$$

where we have neglected parallel temperature for ions and perpendicular temperature for both species. From these equations, we wish to obtain the dielectric tensor, $\vec{\epsilon}$. As exemplified by Stix,[52] we break the equations into components and change coordinates to obtain $\epsilon_\perp$: $v_+\equiv v_x+iv_y$, $v_-\equiv v_x-iv_y$, and similarly for $E_\pm$. Taking appropriate linear combinations of Eqs. (A1) and (A2), we obtain after Fourier analysis

$$v_{e\pm}=\frac{ieE_\pm}{m_e}\frac{1}{\omega+i\nu\mp\Omega_e}$$

for electron motion, and

$$v_{i\pm}=\frac{-ieE_\pm}{m_e}\frac{1}{\omega+i\nu\pm\Omega_i}$$

for ions. We may now use these expressions for v in the generalized Ohm's law,

$$\mathbf{J}_s=n_e q_s \mathbf{v}_s=\vec{\sigma}\mathbf{E}=\frac{-i\omega}{4\pi}\vec{\chi}_s\mathbf{E}, \tag{A3}$$

where q_s and $\vec{\chi}_s$ are the algebraic charge and plasma susceptibility tensor of species s, to obtain $\chi_{e\pm}=\omega_{pe}^2/\omega(\omega+i\nu\mp\Omega_{ce})$, and $\chi_{i\pm}=\omega_{pi}^2/\omega(\omega+i\nu\pm\Omega_{ci})$.

Previous experiments[53,54] in the LAPD have shown that losses due to perpendicular collisions under these conditions are negligible, so the $i\nu$ term in the above equations can be

neglected. Furthermore, since $\omega \ll \Omega_e$, we may set $\omega/\Omega_e \rightarrow 0$. With these approximations, transforming back to xy coordinates, and using

$$\overleftrightarrow{\epsilon}(\omega,\mathbf{k}) = \overleftrightarrow{I} + \sum_s \overleftrightarrow{\chi}_s(\omega,\mathbf{k}), \tag{A4}$$

we may solve for all perpendicular components of $\overleftrightarrow{\epsilon}$.

Obtaining the χ_{zz} term is easier than the perpendicular terms. We first take the $\hat{z}$ component of Eqs. (A1) and (A2). Since the electron thermal speed is faster than the wave phase velocity, the time for parallel electron heat diffusion is small compared to a wave period, and so we can model the electron response as isothermal, i.e., $p_e = n_1 \kappa T_e$. We get, after Fourier analysis

$$v_{ez} = -\frac{e n_0 E_z + i k_\parallel n_1 \kappa T_e}{m_e n_0(\nu - i\omega)}, \tag{A5}$$

and

$$v_{iz} = \frac{e n_0 E_z}{m_i n_0(\nu - i\omega)}. \tag{A6}$$

The first-order density term is eliminated from Eq. (A5) by means of the fluid continuity equation. After using Eq. (A3) to solve for the susceptibilities of each species and putting the results in Eq. (A4), we obtain, after neglecting ω_{pi}^2 relative to ω_{pe}^2, the dielectric tensor $\overleftrightarrow{\epsilon}$

$$\begin{pmatrix} \dfrac{c^2}{v_A^2(1-\overline{\omega^2})} & \dfrac{i\overline{\omega}c^2}{v_A^2(1-\overline{\omega^2})} & 0 \\ \dfrac{-i\overline{\omega}c^2}{v_A^2(1-\overline{\omega^2})} & \dfrac{c^2}{v_A^2(1-\overline{\omega^2})} & 0 \\ 0 & 0 & -\dfrac{\omega_{pe}^2}{\omega^2 - v_e^2 k_\parallel^2 + i\omega\nu} \end{pmatrix}. \tag{A7}$$

A slightly different version of this dielectric tensor was obtained by Donnelly.[55]

Using Faraday's law and $\nabla \times \mathbf{B} = -i(\omega/c)\overleftrightarrow{\epsilon}\mathbf{E}$, we can eliminate two components from the unknowns E_r, E_ϕ, E_z, B_r, B_ϕ, B_z. Since our waves do not exhibit azimuthal dependence, we will set $m = 0$. Also, noting that $\epsilon_{rr} = \epsilon_{\phi\phi}$, and $\epsilon_{r\phi} = -\epsilon_{\phi r}$ from Eq. (A7), we can write the following equations:

$$\frac{1}{r}\frac{\partial(rE_\phi)}{\partial r} = i\frac{\omega^2}{c^2}B_z, \tag{A8}$$

$$\frac{1}{r}\frac{\partial(rB_\phi)}{\partial r} = -\frac{i\omega}{c}\epsilon_{zz}E_z, \tag{A9}$$

$$\epsilon_{rr}\frac{i\omega}{c}\frac{\partial E_z}{\partial r} = \frac{i\omega}{c}k_\parallel \epsilon_{r\phi}E_\phi + \left(\frac{\omega^2}{c^2}\epsilon_{rr} - k_\parallel^2\right)B_\phi, \tag{A10}$$

$$\frac{\partial B_z}{\partial r} = \left[\left(\frac{i\omega}{c}\epsilon_{rr} - \frac{ick_\parallel^2}{\omega}\right) - \frac{i\omega}{c}\frac{\epsilon_{r\phi}^2}{\epsilon_{rr}}\right]E_\phi + k_\parallel \frac{\epsilon_{r\phi}}{\epsilon_{rr}}B_\phi. \tag{A11}$$

One of the more ubiquitous methods for solving waveguide problems[49,56,57] and plasma-filled waveguide problems[52,58] is to acquire differential equations for transverse and longitudinal components solely in terms of the longitudinal component. This is what we embark upon first.

In order to isolate the wave B_z, we will have to take four derivatives of Eq. (A11), eliminating each time the first-order derivatives of the other field quantities that appear using Eqs. (A8)–(A10). In a cylindrical geometry we expect that the z component of the wave magnetic field will solve a Bessel-type differential equation. With this in mind, we first apply the operator $(1/r)(\partial/\partial r)r$ to Eq. (A11) and substitute for the $(1/r)\partial/\partial r(rE_\phi)$ and $(1/r)\partial/\partial r(rB_\phi)$ terms that appear to get

$$\frac{1}{r}\frac{\partial}{\partial r}\left(r\frac{\partial B_z}{\partial r}\right) = \frac{i\omega}{c}\left[\left(\frac{i\omega}{c}\epsilon_{rr} - \frac{ick_\parallel^2}{\omega}\right) - \frac{i\omega}{c}\frac{\epsilon_{r\phi}^2}{\epsilon_{rr}}\right]B_z - \frac{i\omega k_\parallel}{c}\frac{\epsilon_{r\phi}\epsilon_{zz}}{\epsilon_{rr}}E_z. \tag{A12}$$

We proceed in this manner—taking derivatives and substituting for field variables that are not B_z—until we eventually come up against

$$\begin{aligned} \frac{1}{r}\frac{\partial}{\partial r}&\left\{r\frac{\partial}{\partial r}\left[\frac{1}{r}\frac{\partial}{\partial r}\left(r\frac{\partial B_z}{\partial r}\right)\right]\right\} \\ &= \left\{\frac{i\omega}{c}\left[\left(\frac{i\omega}{c}\epsilon_{rr} - \frac{ick_\parallel^2}{\omega}\right) - \frac{i\omega}{c}\frac{\epsilon_{r\phi}^2}{\epsilon_{rr}}\right] - \frac{\epsilon_{zz}}{\epsilon_{rr}}\left(\frac{\omega^2}{c^2}\epsilon_{rr} - k_\parallel^2\right)\right\}\frac{1}{r}\frac{\partial}{\partial r}\left(r\frac{\partial B_z}{\partial r}\right) \\ &+ \left\{\frac{\omega^2 k_\parallel^2}{c^2}\frac{\epsilon_{zz}\epsilon_{r\phi}^2}{\epsilon_{rr}^2} + \frac{\epsilon_{zz}}{\epsilon_{rr}}\left(\frac{\omega^2}{c^2}\epsilon_{rr} - k_\parallel^2\right)\right. \\ &\left.\times\frac{i\omega}{c}\left[\left(\frac{i\omega}{c}\epsilon_{rr} - \frac{ick_\parallel^2}{\omega}\right) - \frac{i\omega}{c}\frac{\epsilon_{r\phi}^2}{\epsilon_{rr}}\right]\right\}B_z. \end{aligned} \tag{A13}$$

The operator on the left-hand side of the = sign of Eq. (A13) is recognized as the radial portion of the ∇^2 operator in cylindrical geometry (which we will denote ∇_r^2) applied twice to B_z. Adapting the method of Woods,[59] we assume that the B_z field variable is an eigenvector of the $m = 0$ Bessel equation and replace the operator ∇_r^2 everywhere it appears with its eigenvalue, $-k_\perp^2$. This gives us an equation quadratic in $k_\perp^2$

$$\epsilon_{rr}k_\perp^4 + \left[(\epsilon_{rr} + \epsilon_{zz})\left(k_\parallel^2 - \frac{\omega^2}{c^2}\epsilon_{rr}\right) + \frac{\omega^2}{c^2}\epsilon_{r\phi}^2\right]k_\perp^2 - \left[\frac{\omega^4}{c^4}\epsilon_{zz}\epsilon_{r\phi}^2 - \epsilon_{zz}\left(\frac{\omega^2}{c^2}\epsilon_{rr} - k_\parallel^2\right)^2\right] = 0. \tag{A14}$$

We may now solve for $k_\perp$ to obtain formula (10) in the text

$$k_\perp^2 = \frac{\left[(\epsilon_{rr}+\epsilon_{zz})\left(\frac{\omega^2}{c^2}\epsilon_{rr}-k_\parallel^2\right)-\frac{\omega^2}{c^2}\epsilon_{r\phi}^2\right]}{2\epsilon_{rr}} \pm \frac{\sqrt{\left[(\epsilon_{rr}+\epsilon_{zz})\left(\frac{\omega^2}{c^2}\epsilon_{rr}-k_\parallel^2\right)-\frac{\omega^2}{c^2}\epsilon_{r\phi}^2\right]^2-4\epsilon_{rr}\epsilon_{zz}\left[\left(\frac{\omega^2}{c^2}\epsilon_{rr}-k_\parallel^2\right)^2-\frac{\omega^4}{c^4}\epsilon_{r\phi}^2\right]}}{2\epsilon_{rr}}. \quad \text{(A15)}$$

[1] A. Hasegawa and C. Uberoi, *The Alfvén Wave* (Technical Information Center, U. S. Department of Energy, Springfield, VA, 1982).
[2] A. Y. Tsushima, Y. Amagishi, and M. Inutake, Phys. Lett. A **88**, 457 (1982).
[3] M. Cekic, B. A. Nelson, and F. L. Ribe, Phys. Fluids B **4**, 392 (1992).
[4] R. Behn, A. de Chambrier, G. A. Collins *et al.*, Plasma Phys. Controlled Fusion **26**, 173 (1984).
[5] G. J. Kramer, M. Saigusa, T. Ozeki, Y. Kusama, H. Kimura, T. Oikawa, K. Tobita, G. Y. Fu, and C. Z. Cheng, Phys. Rev. Lett. **80**, 2594 (1998).
[6] M. J. Engebretson, L. J. Zanetti, T. A. Potemra, and M. H. Acuna, Geophys. Res. Lett. **13**, 905 (1986).
[7] R. A. Mathie, F. W. Menk, I. R. Mann, and D. Orr, Geophys. Res. Lett. **26**, 659 (1999).
[8] M. R. Lessard, M. K. Hudson, J. C. Samson, and J. R. Wygant, J. Geophys. Res. **104**, 12361 (1999).
[9] K. Takahashi and R. L. McPherron, Planet. Space Sci. **32**, 1343 (1984).
[10] J. C. Samson, D. D. Wallis, T. J. Hughes, F. Creutzberg, J. M. Ruohoniemi, and R. A. Greenwald, J. Geophys. Res. **97**, 8495 (1992).
[11] B.-L. Xu, J. C. Samson, W. W. Liu, F. Creutzberg, and T. J. Hughes, J. Geophys. Res. **98**, 11531 (1993).
[12] A. V. Streltsov, W. Lotko, J. R. Johnson, and C. Z. Cheng, J. Geophys. Res. **103**, 26559 (1998).
[13] J. C. Samson, L. L. Cogger, and Q. Pao, J. Geophys. Res. **101**, 17373 (1996).
[14] M. G. Kivelson and D. J. Southwood, Geophys. Res. Lett. **12**, 49 (1985).
[15] J. C. Samson, D. D. Wallis, T. J. Hughes, F. Creutzberg, J. M. Ruohoniemi, and R. A. Greenwald, Geophys. Res. Lett. **19**, 441 (1992).
[16] P. J. Hansen and C. K. Goertz, Phys. Fluids B **4**, 2713 (1992).
[17] M. J. Thompson and A. N. Wright, Phys. Plasmas **1**, 1092 (1994).
[18] E. N. Fedorov, N. G. Mazur, V. A. Pilipenko, and K. Yumoto, Phys. Plasmas **2**, 527 (1995).
[19] W. J. Tirry and M. Goossens, J. Geophys. Res. **100**, 23687 (1995).
[20] N. Bentenitis, Grad Life, The Newsletter of the Graduate Council at Rensselaer **2**, 1 (2000).
[21] P. M. Bellan, Phys. Plasmas **1**, 3523 (1994).
[22] J. P. Goedbloed and A. Lifschitz, Phys. Plasmas **2**, 3550 (1995).
[23] M. S. Ruderman, M. Goossens, and I. Zhelyazkov, Phys. Plasmas **2**, 3547 (1995).
[24] S. Rauf and J. A. Tataronis, Phys. Plasmas **2**, 340 (1995).
[25] P. M. Bellan, Phys. Plasmas **3**, 435 (1996).
[26] P. M. Bellan, J. Geophys. Res. **101**, 24887 (1996).
[27] A. N. Wright and W. Allan, J. Geophys. Res. **101**, 24991 (1996).
[28] M. Goossens, M. S. Ruderman, and J. V. Hollweg, Sol. Phys. **157**, 75 (1995).
[29] W. J. Tirry and M. Goossens, Astrophys. J. **471**, 501 (1996).
[30] E. M. Poulter, W. Allan, J. G. Keys, and E. Nielsen, Planet. Space Sci. **32**, 1069 (1984).
[31] M. Volwerk, M. G. Kivelson, K. K. Khurana, and R. L. McPherron, J. Geophys. Res. **104**, 14729 (1999).
[32] C. T. Russell, Geophys. Res. Lett. **16**, 1253 (1989).
[33] H. J. Singer, W. J. Hughes, and C. T. Russell, J. Geophys. Res. **87**, 3519 (1982).
[34] W. Gekelman, H. Pfister, Z. Lucky, J. Bamber, D. L. Leneman, and J. Maggs, Rev. Sci. Instrum. **62**, 2875 (1991).
[35] P. Stangeby, in *Plasma Diagnostics*, edited by O. Auciello and D. L. Flamm (Boston Academic, Boston, MA, 1989).
[36] M. A. Gilmore, W. A. Peebles, and X. V. Nguyen, Plasma Phys. Controlled Fusion **42**, L1 (2000).
[37] G. J. Morales and J. E. Maggs, Phys. Plasmas **4**, 4118 (1997).
[38] W. Gekelman, S. Vincena, and D. Leneman, Plasma Phys. Controlled Fusion **39**, 101 (1997).
[39] D. Leneman, W. N. Gekelman, and J. E. Maggs, Phys. Plasmas **7**, 3934 (2000).
[40] L. Mandrake and W. Gekelman, Comput. Phys. **11**, 498 (1997).
[41] C. C. Mitchell, S. V. Vincena, J. E. Maggs, and W. N. Gekelman, Geophys. Res. Lett. **28**, 923 (2001).
[42] A. Streltsov and W. Lotko, J. Geophys. Res. **101**, 5343 (1996).
[43] J. V. Hollweg, J. Geophys. Res. **104**, 14811 (1999).
[44] G. Arfken, *Mathematical Methods for Physicists* (Academic, Orlando, 1985).
[45] A. Battacharjee, C. A. Kletzing, Z. W. Ma, C. S. Ng, N. F. Otani, and X. Wang, Geophys. Res. Lett. **26**, 3281 (1999).
[46] W. Gekelman, S. Vincena, D. Leneman, and J. Maggs, J. Geophys. Res. **102**, 7225 (1997).
[47] R. Lysak and W. Lotko, J. Geophys. Res. **101**, 5085 (1996).
[48] Y. M. Voitenko, Sol. Phys. **182**, 411 (1998).
[49] J. D. Jackson, *Classical Electrodynamics*, 2nd ed. (Wiley, New York, 1975).
[50] R. A. Koch and W. Horton, Jr., Phys. Fluids **18**, 861 (1975).
[51] G. J. Morales (unpublished).
[52] T. H. Stix, *Waves in Plasmas* (McGraw-Hill, New York, 1992).
[53] S. T. Vincena and W. N. Gekelman, IEEE Trans. Plasma Sci. **27**, 144 (1999).
[54] D. Leneman, Ph.D. thesis, University of California at Los Angeles, 1998.
[55] I. J. Donnelly and B. E. Clancy, Aust. J. Phys. **36**, 305 (1983).
[56] M. Schwartz, *Principles of Electrodynamics* (McGraw-Hill, New York, 1972).
[57] D. J. Griffiths, *Introduction to Electrodynamics* (Prentice-Hall, Englewood Cliffs, NJ, 1989).
[58] D. G. Swanson, *Plasma Waves* (Academic, San Diego, 1989).
[59] L. C. Woods, J. Fluid Mech. **13**, 570 (1962).